# MULTI-PERFORMANCE OPTIMIZATION OF THE LIQUID $CO_2$-ASSISTED MINIMUM QUANTITY LUBRICATION ROLLER BURNISHING PROCESS IN TERMS OF COEFFICIENT OF FRICTION AND PARTICULATE MATTER

**Le Tuan Vu[1], Le Van Luan[1], Bui Huu Toan[1], Do Manh Tung[1], Nguyen Trung Thanh[1,*]**

DOI: https://doi.org/10.57001/huih5804.2026.008

**ABSTRACT**

In this study, a hybrid cooling system comprising the liquid $CO_2$ and minimum quantity lubrication (MQL) is proposed to facilitate the flat roller burnishing process of the SKD61 steel. The operating parameters, including the air pressure (*P*), lubricant flow rate (*L*), and $CO_2$ flow rate (*C*) were optimized to reduce the coefficient of friction (*COF*) and particulate matter 10 concentration (*PM10*). The Extreme Gradient Boosting (OXGBoost), the method used the removal effects of criteria (MEREC), and the dragonfly algorithm (DA) are utilized to find optimized solutions. The findings presented that the optimized outcomes of the *P*, *L*, and *C* are 0.6MPa, 150ml/h, and 17L/min. The *COF* and *PM10* were decreased by 5.9% and 22.3%, respectively, as compared to the user-defined values. The MQL produces significantly the particulate matter 10 concentration, while the liquid $CO_2$ generates the *PM10* under the impact of the machining temperature. The *COF* of the burnished surface was effectively decreased, as compared to the milled one. The obtained results can be efficiently used to enhance surface properties and reduce the air pollution.

***Keywords:*** *Liquid $CO_2$; minimum quantity lubrication; particulate matter 10; machine learning; Dragonfly algorithm.*

[1]Faculty of Mechanical Engineering, Le Quy Don Technical University, Vietnam
[*]Email: trungthanhk21@mta.edu.vn
Received: 04/9/2025
Revised: 08/01/2026
Accepted: 28/01/2026

## 1. INTRODUCTION

The burnishing process is extensively used to produce a smooth surface finish, in which the specimen's surface is processed using the machined pressure. This operation is performed without removing material from the workpiece. The roughness was efficiently decreased, while the hardness and residual stress were effectively enhanced due to the reduction of the surface irregularities. Consequently, the burnishing operation could be effectively utilized to burnish different surfaces and materials.

Recently, advanced cooling lubrication approaches, including the MQL, cold, and cryogenic techniques were suggested and used to improve the performance outcomes of different burnishing operations. Rotella et al. emphasized that a lower roughness of the burnished Ti6Al4V could be obtained using the MQL [1]. Nguyen et al. found that the energy and roughness of the burnished AISI-5145 were reduced by 11.8% and 13.8%, respectively, using optimal MQL parameters [2]. Cagan et al. indicated that the burnished hardness was mainly affected by the force, feed, and passes, respectively [3]. Cagan presented that the lower roughness of the compressed Al8090 could be obtained at the MQL condition [4]. Nguyen et al. emphasized that the MQL was a prominent approach to improve the machined roughness and hardness of the compressed AISI 4140 [5]. The Vortex tube-assisted MQL was developed to facilitate the external burnishing, in which the tribological indicators were significantly improved [6]. The machined roughness and hardness of the $LN_2$-burnished 17-4 stainless were improved by 36.8% and 42.6%, as compared to the untreated specimen [7]. The burnished hardness was enhanced by 29.7% using the liquid $LN_2$, as compared to the dry condition, while the nano-grain was found in the burnished region [8]. The

liquid $CO_2$ and Vortex tube were combined to facilitate the internal burnishing operation, in which the roughness and energy were enhanced by 4.0% and 20.3%, respectively [9]. Maximov et al. presented that the cryogenic condition was utilized to produce the highest hardness and residual stress on the burnished chromium-nickel stainless [10]. The optimized outcomes of the *P*, *L*, and nozzle diameter of the cold burnishing process were selected to improve outcomes measured [11]. The results indicated that the energy and roughness were reduced by 9.1% and 1.5%, respectively. Maximov stated that the fatigue strength and compressive residual stress of the LN2-burnished SS304 were enhanced by 35.2% and 242.8%, compared to the untreated specimen [12]. Sachin et al. indicated that the burnished hardness of the processed 17-4 PH was increased by 4% using the smallest tool [13]. The processed hardness of the machined Mg-4Zn-1Sr was improved by 54% using cryogenic ball burnishing, as compared to the untreated sample [14]. Hou et al. indicated that the roughness and thickness of the burnished layer of the $LN_2$-processed Ti6Al4V were 0.117µm and 300µm, respectively [15]. However, the drawbacks of the related publications can be stated as below.

Firstly, a novel cooling lubrication method combining liquid $CO_2$ and MQL (LCMQL) has not been developed in published works. Secondly, the influences of the LCMQL parameters on the *COF* and *PM10* have not been explored. Thirdly, the *COF* and *PM10* models in terms of the LCMQL parameters have not been developed. Finally, the optimal LCMQL parameters have not been selected to improve the performance outcomes.

The materials and methods are then presented. After that, a description of the results follows. Lastly, the research findings are shown.

## 2. OPTIMIZATION APPROACH

### 2.1. Burnishing parameters and responses

Fig. 1 presents the LCMQL factors and burnishing responses, in which the in which the *COF* and *PM10* are considered and optimized.

The *COF* is computed as:

$$COF = \frac{\sum_{i}^{n} COF_i}{n} \quad (1)$$

where $COF_i$ denotes the coefficient of friction at the $i_{th}$ time.

The *PM10* is computed as:

$$PM10 = \frac{\sum_{i}^{n} PM10_i}{n} \quad (2)$$

where $PM10_i$ is the particulate matter 10 concentration at $i_{th}$ time.

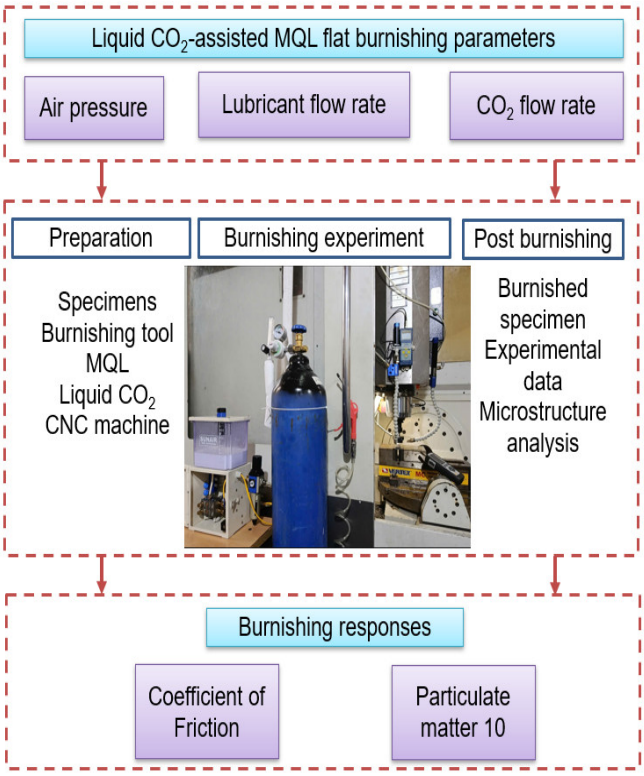


Figure 1. LCMQL factors and responses

Three key operating factors, including the *P*, *L*, *C*, and their ranges are shown in Table 1. The *P* and *L* values are selected with the aid of the MQL system's recommendations. The *C* value is chosen using the user's guide of the liquid tank. Therefore, the mathematical optimization is expressed as:

Finding optimal LCMQL parameters = [*P*, *L*, and *C*].

Optimization: $f(X) = \omega_1 COF + \omega_2 PM10$

where $\omega_i$ is the weight of the $i_{th}$ burnishing response.

Minimizing *COF* and *PM10*.

Constraints: $0.2 \le P \le 0.6$MPa; $100 \le L \le 200$ml/h; $15 \le C \le 25$L/min.

Table 1. The operating parameters of the hybrid cooling system

| No. | Symbol | Parameters | Levels | Unit |
|---|---|---|---|---|
| 1 | *P* | Air pressure | 0.2-0.4-0.6 | MPa |
| 2 | *L* | Lubricant flow rate | 100-150-200 | ml/h |
| 3 | *C* | $CO_2$ flow rate | 15-20-25 | L/min |

### 2.2. Optimization method

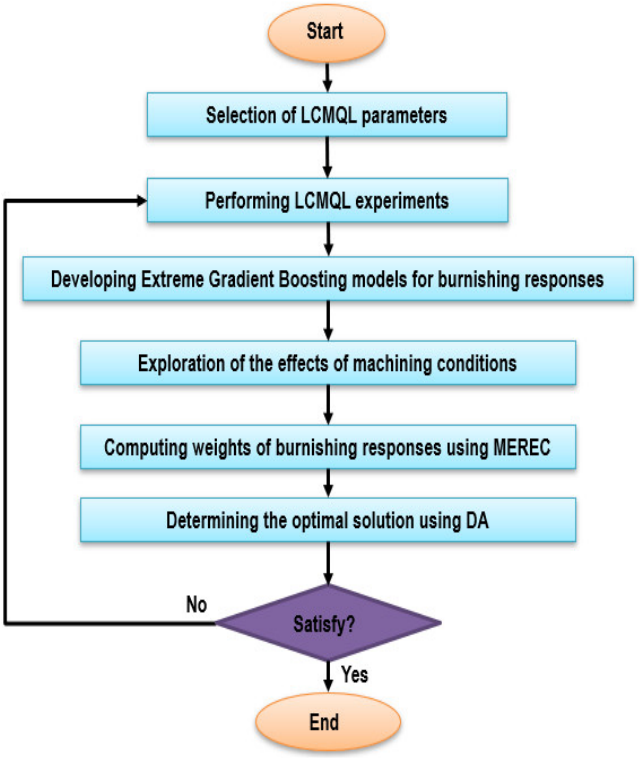


Figure 2. Optimization approach for the burnishing process

The optimization sequence for the burnishing process is depicted in Fig. 2:

Step 1: Performing burnishing trials with three levels of inputs; hence, a total of 27 experiments are performed [16].

Step 2: The MEREC is utilized to compute the performance outcome's weight [17].

In terms of a higher purpose, the burnishing performance outcome ($n_{ij}$) is normalized as:

$$n_{ij} = \frac{\min y_i}{y_i} \tag{3}$$

In terms of a lower purpose, the burnishing performance outcome ($n_{ij}$) is normalized as:

$$n_{ij} = \frac{y_i}{\max y_i} \tag{4}$$

The performance of the alternative solution ($AS_i$) is calculated as:

$$AS_i = \ln[1+(\frac{1}{NO}\sum_j \left|\ln(n_{ij})\right|)] \tag{5}$$

where $NO$ demotes the numbers of burnishing objectives.

The performance of the remaining criterion ($RS'_{ij}$) is calculated as:

$$RS'_{ij} = \ln[1+(\frac{1}{NR}\sum_{k,k\neq j} \left|\ln(n_{ij})\right|)] \tag{6}$$

where $NR$ demotes the numbers of remaining burnishing objectives.

The removal impact of the performance outcome ($R_i$) is computed as:

$$R_i = \sum_i \left| S'_{ij} - S_i \right| \tag{7}$$

The weight ($\omega_i$) is computed as:

$$\omega_i = \frac{R_i}{\sum_{k=1}^{n} R_k} \tag{8}$$

Step 3: The OXGBoost is ultilized to propose the burnishing models [18].

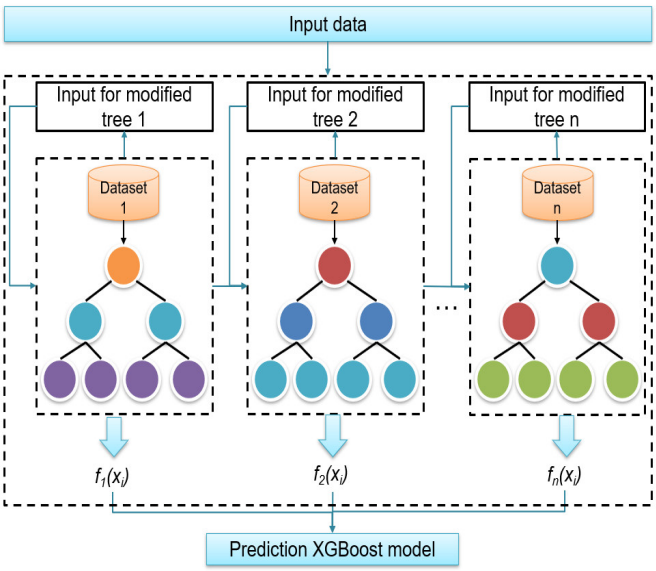


Figure 3. The scheme of the XGBoost model

The structure of the XGBoost model having classification and regression trees (CARTs) is presented in Fig. 3, in which each CART contains the root nodes, internal nodes, leaf nodes, and branches. The inputs are firstly imported into the root node to make the original decision. The internal nodes are then to make subsequent decision. The leaf nodes represent the prediction results of a single classification and regression tree. The results of all leaf-pointing nodes are combined to obtain the prediction results of the XGBoost model. The XGBoost model is expressed as:

$$\widehat{y_i} = \alpha \sum_{k=1}^{n} f_k(x_i) \tag{9}$$

where $x_i$ is the input data. $\alpha$ is the learning rate of the individual regression tree, $n$ is the total number of CARTs, $f_k$ is the output of the $k_{th}$ regression tree.

The model's outcome is evaluated using the objective function ($L$) which is expressed as:

$$L = \sum_{i}^{n} l_k(y_i, \widehat{y_i}) + \sum_{k=1}^{K} \Omega(f_x) \quad (10)$$

where $l_k$ and $\Omega$ are the loss function and regularization item, respectively. For each CART, the regularization item is expressed as:

$$\Omega(f) = \gamma T + \frac{1}{2}\lambda \|w\|^2 \quad (11)$$

where $T$ is the number of leaves. $\gamma$ and $\lambda$ are penalty coefficients. $w$ is a vector presenting the score of each leaf.

Step 4: The dragonfly algorithm (DA) is used to find the optimal solution. The DA is developed based on the natural dynamic (migratory) and static (feeding) swarming behaviors of dragonflies, which contain the exploitation and exploration phases (Fig. 4). In the exploitation phase, the dragonflies make the swarms migrate in one direction over long distances and distract from enemies (Fig. 5). In the exploration phase, dragonflies form small groups and enter a small area to search for food and attract flying prey.

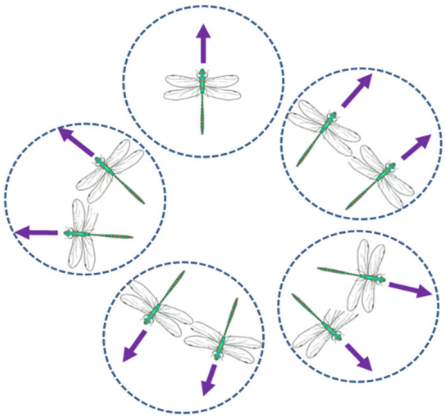

Figure 4. The static behavior of the dragonfly algorithm

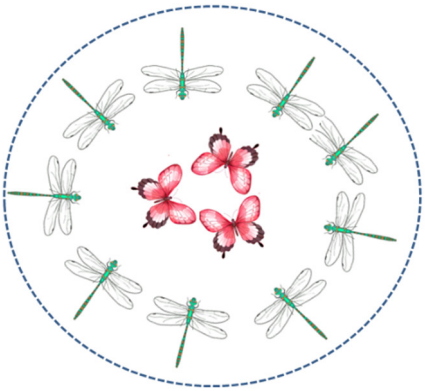

Figure 5. The dynamic behavior of the dragonfly algorithm

The DA having five basic principles are expressed as follows:

The separation process is used to prevent static collisions among individuals. The separation is expressed as:

$$S_i = -\sum_{j-1}^{M} P - P_j \quad (12)$$

where $P$ and $P_j$ are the positions of the current individual and its neighboring individual. $M$ is the number of individuals in the design space.

The alignment process is used to present the velocity matching among individuals in the design space. The alignment is expressed as:

$$A_i = \frac{\sum_{j-1}^{M} V_j}{M} \quad (13)$$

where $V_j$ denotes the velocity of the $j_{th}$ neighboring individual.

The cohesion is used to present the tendency of individuals toward the center of the mass of the neighborhood. The cohesion is expressed as:

$$A_i = \frac{\sum_{j-1}^{M} P_j}{M} - P \quad (14)$$

The attraction process is used to find the food source ($F_i$). The attraction is expressed as:

$$F_i = F_p - P \quad (15)$$

where $F_p$ is the position of the food source.

The distraction process is used to escape from the enemies. The distraction is expressed as:

$$E_i = E_p + P \quad (16)$$

where $E_i$ denotes the position of the enemy of the $i_{th}$ individual and $E_p$ denotes the enemy's position.

The updated position of the individual is expressed as:

$$P_i^{t+1} = \Delta P_i^{t+1} + P_i^t \quad (17)$$

where $\Delta P$ is the step vector and expressed as:

$$\Delta P_i^{t+1} = (sS_i + aA_i + cC_i + fF_i + eE_i) + \beta \Delta P_i^t \quad (18)$$

where $S_i$, $A_i$, $C_i$, and $E_i$ are the separation, the alignment, the cohesion, and the enemy of the $i_{th}$ individual, respectively. $s$, $a$, $c$, $f$, $e$, and $\beta$ are the swarming factors.

The updated position of the $i_{th}$ dragonfly is as follows:

$$P_i^{t+1} = P_i^t + Levy(d) \times P_i^t \quad (19)$$

where $d$ represents the dimension of the position vectors. The Levy flight is expressed as:

$$Levy(d) = 0.01 \times \frac{r_1 \times \sigma}{|r_2|^{\frac{1}{\beta}}} \quad (20)$$

where $r_1$ and $r_2$ are random vectors uniformly distributed in the range [0,1].

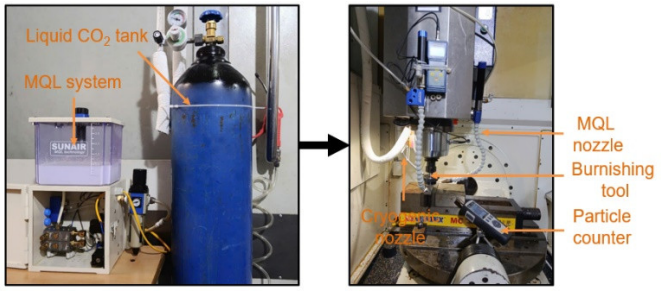


(a) Burnishing operation

(b) Measuring friction of coefficient

Figure 6. The experimental setting

Table 2. Chemical compositions of the SKD 61 steel

| Elements | C | Si | Mn | P | S | Cr | Mo | V |
|---|---|---|---|---|---|---|---|---|
| % | 0.42 | 1.2 | 0.50 | 0.03 | 0.02 | 5.50 | 1.50 | 1.15 |

## 3. EXPERIMENTAL SETTING

The SKD61 extensively used in manufacturing dies and molds is chosen as the burnishing specimen. Table 2 displays the chemical compositions of the SKD61. Each workpiece measures 180.0mm in length, 30.0mm in width, and 12.0mm in thickness. The spindle speed of 360rpm, feed rate of 200mm/min, depth of cut of 0.15mm, and number of paths of 2 are utilized for the milling operation. The *P* and *L* for the milling process are 0.4MPa and 100ml/h, respectively.

To conduct experiments, a burnishing tool with six movable rollers and an average diameter of 40.0mm is used (Fig. 6a). New rollers are installed after each trial. The spindle speed of 1400rpm, feed rate of 100mm/min, and depth of penetration of 0.14mm are used for each trial. Two MQL nozzles and a cryogenic one are utilized. The nozzles are evenly spaced on a circular cross-section, and the angle between the nozzles is 120°. The lubricant and liquid $CO_2$ are simultaneously transferred into the interfaces to produce the thin film. The particle counter entitled CEMDT-9850M is used to measure the *PM10* in a duration of 20 seconds.

The tribometer entitled CETR-UMT2 is applied to measure the friction of coefficient at a constant load of 25N and a constant sliding time of 1000s (Fig. 6b). The temperature and humidity lie are 25°C and 63%, respectively. The *COF* of the milled surface is 0.753.

The *COF* and *PMI* at different LCMQL conditions are presented in Figs. 7 and 8.

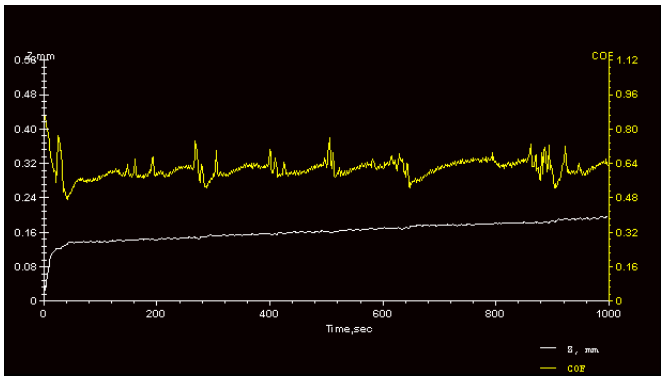


(a) COF at the No. 6


(b) PM10 at the No. 6

Figure 7. The burnishing responses at the No. 6

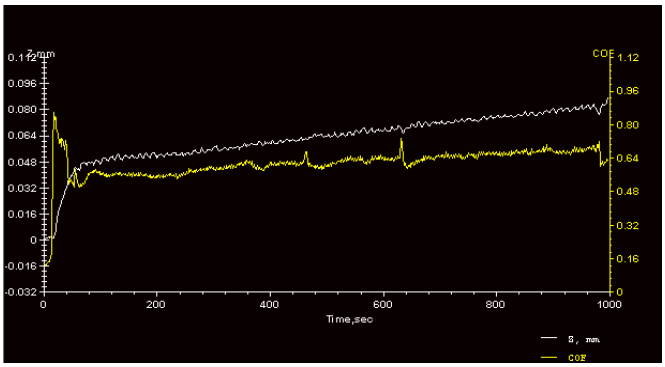


(a) COF at the No. 12


(b) PM10 at the No. 12

Figure 8. The burnishing responses at the No. 12

## 4. RESULTS AND DISCUSSIONS

The experimental outcomes of the burnishing responses are exhibited in Table 3.

### 4.1. The ANOVA results

The ANOVA is used to test the model's adequacy and significant factors. For the *COF* model, the values of the $R^2$ value (0.9864), the adjusted $R^2$ (0.9674), and the predicted $R^2$ (0.9538) indicate that the *COF* model is adequate (Table 4). The counted contributions of the *P*, *L*, and *C* are 19.79%, 21.53%, and 17.14%, respectively. The counted contribution of the PL, *LC*, and LC are 4.78%, 4.06%, and 6.46%, respectively. The counted contributions of the $P^2$, $L^2$, and $C^2$ are 6.59%, 10.86%, and 8.79%, respectively.

The ANOVA results of the *PM10* model are shown in Table 5. For the *PM10* correlation, the values of the $R^2$ value (0.9842), the adjusted $R^2$ (0.9732), and the predicted $R^2$ (0.9645) indicate that the *PM10* model is adequate. The counted contributions of the *P*, *L*, and *C* are 15.61%, 22.07%, and 19.38%, respectively. The counted contributions of the *PL*, *PC*, and *LC* are 12.24%, 1.72%, and 13.04%, respectively. The counted contributions of the $P^2$, $L^2$, and $C^2$ are 3.91%, 9.90%, and 2.13%, respectively.

Fig. 9 presents the comparisons betwen the predicted and actual values for burnishing responses. The data are distributed on the straight lines, presenting the model's adequacy.

Table 3. Experimental results of the **burnishing** operation

| No. | *P* (MPa) | *L* (ml/h) | *C* (L/min) | *COF* | *PM10* (μg/m³) |
|---|---|---|---|---|---|
| 1 | 0.2 | 100 | 15 | 0.689 | 3452 |
| 2 | 0.4 | 100 | 15 | 0.681 | 9136 |
| 3 | 0.6 | 100 | 15 | 0.646 | 13339 |
| 4 | 0.2 | 150 | 15 | 0.623 | 10538 |
| 5 | 0.4 | 150 | 15 | 0.605 | 13906 |
| 6 | 0.6 | 150 | 15 | 0.562 | 15704 |
| 7 | 0.2 | 200 | 15 | 0.599 | 21372 |
| 8 | 0.4 | 200 | 15 | 0.572 | 22424 |
| 9 | 0.6 | 200 | 15 | 0.519 | 21995 |
| 10 | 0.2 | 100 | 20 | 0.634 | 9655 |
| 11 | 0.4 | 100 | 20 | 0.618 | 15666 |
| 12 | 0.6 | 100 | 20 | 0.576 | 20321 |
| 13 | 0.2 | 150 | 20 | 0.581 | 14273 |
| 14 | 0.4 | 150 | 20 | 0.555 | 17968 |
| 15 | 0.6 | 150 | 20 | 0.504 | 20182 |
| 16 | 0.2 | 200 | 20 | 0.569 | 22638 |
| 17 | 0.4 | 200 | 20 | 0.534 | 24017 |
| 18 | 0.6 | 200 | 20 | 0.474 | 23915 |
| 19 | 0.2 | 100 | 25 | 0.613 | 15068 |
| 20 | 0.4 | 100 | 25 | 0.589 | 21406 |
| 21 | 0.6 | 100 | 25 | 0.536 | 26263 |
| 22 | 0.2 | 150 | 25 | 0.572 | 17218 |
| 23 | 0.4 | 150 | 25 | 0.539 | 21241 |
| 24 | 0.6 | 150 | 25 | 0.481 | 23781 |
| 25 | 0.2 | 200 | 25 | 0.573 | 23115 |
| 26 | 0.4 | 200 | 25 | 0.531 | 24821 |
| 27 | 0.6 | 200 | 25 | 0.463 | 25046 |

Table 4. ANOVA results for the COF model

| Source | Sum of Squares | Mean Square | F Value | p-value | Contri. (%) | Remark |
|---|---|---|---|---|---|---|
| Model | 0.03885 | 0.00432 | 56.41 | < 0.0001 | | Significant |
| *P* | 0.00769 | 0.00769 | 96.11 | < 0.0001 | 19.79 | Significant |
| *L* | 0.00836 | 0.00836 | 104.56 | < 0.0001 | 21.53 | Significant |
| *C* | 0.00666 | 0.00666 | 83.24 | < 0.0001 | 17.14 | Significant |
| *PL* | 0.00186 | 0.00186 | 23.21 | 0.0005 | 4.78 | Significant |
| *PC* | 0.00158 | 0.00158 | 19.72 | 0.0006 | 4.06 | Significant |
| *LC* | 0.00251 | 0.00251 | 31.37 | 0.0004 | 6.46 | Significant |
| $P^2$ | 0.00256 | 0.00256 | 32.00 | 0.0003 | 6.59 | Significant |
| $L^2$ | 0.00422 | 0.00422 | 52.74 | < 0.0001 | 10.86 | Significant |
| $C^2$ | 0.00341 | 0.00341 | 42.69 | < 0.0001 | 8.79 | Significant |
| Residual | 0.00054 | 0.00008 | | | | |
| Cor Total | 0.03939 | | | | | |
| $R^2 = 0.9864$; Adj. $R^2 = 0.9674$; Pred. $R^2 = 0.9538$ | | | | | | |

Table 5. ANOVA results for the PM10 model

| Source | Sum of Squares | Mean Square | F Value | p-value | Contri. (%) | Remark |
|---|---|---|---|---|---|---|
| Model | 375860788.87 | 41762309.87 | 48.45 | < 0.0001 | | Significant |
| *P* | 58671869.14 | 58671869.14 | 68.07 | < 0.0001 | 15.61 | Significant |
| *L* | 82952476.10 | 82952476.10 | 96.23 | < 0.0001 | 22.07 | Significant |
| *C* | 72841820.88 | 72841820.88 | 84.50 | < 0.0001 | 19.38 | Significant |
| *PL* | 46005360.56 | 46005360.56 | 53.37 | < 0.0001 | 12.24 | Significant |
| *PC* | 6464805.57 | 6464805.57 | 7.50 | 0.0006 | 1.72 | Significant |
| *LC* | 49012246.87 | 49012246.87 | 56.86 | < 0.0001 | 13.04 | Significant |
| $P^2$ | 14696156.84 | 14696156.84 | 17.05 | 0.0003 | 3.91 | Significant |
| $L^2$ | 37210218.10 | 37210218.10 | 43.17 | < 0.0001 | 9.90 | Significant |
| $C^2$ | 8005834.80 | 8005834.80 | 9.29 | 0.0005 | 2.13 | Significant |
| Residual | 6033936.66 | 861990.95 | | | | |
| Cor Total | 381894725.53 | | | | | |
| $R^2 = 0.9842$; Adj. $R^2 = 0.9732$; Pred. $R^2 = 0.9646$ | | | | | | |

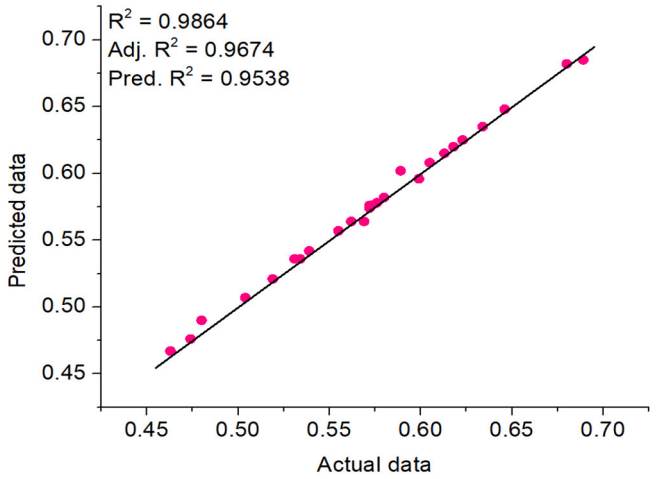


(a) For COF model

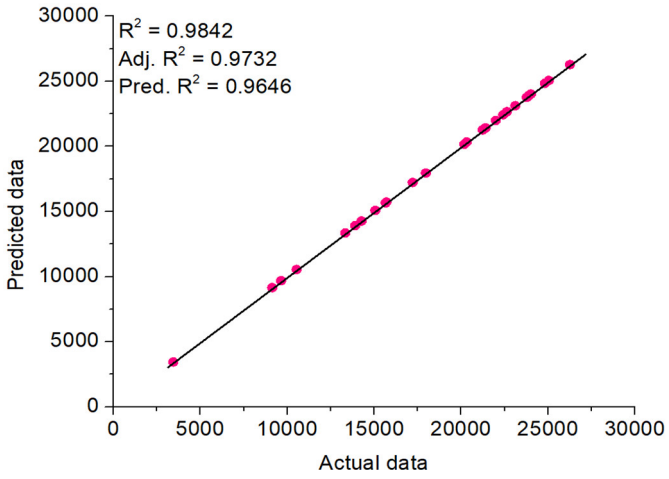


(b) For PM10 model

Figure 9. Comparisons betwen the predicted and actual values for burnishing responses

## 4.2. The parametric impacts

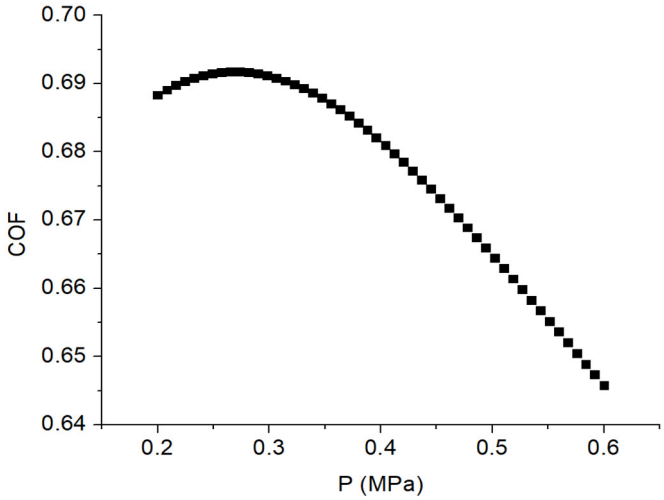


(a) COF versus P

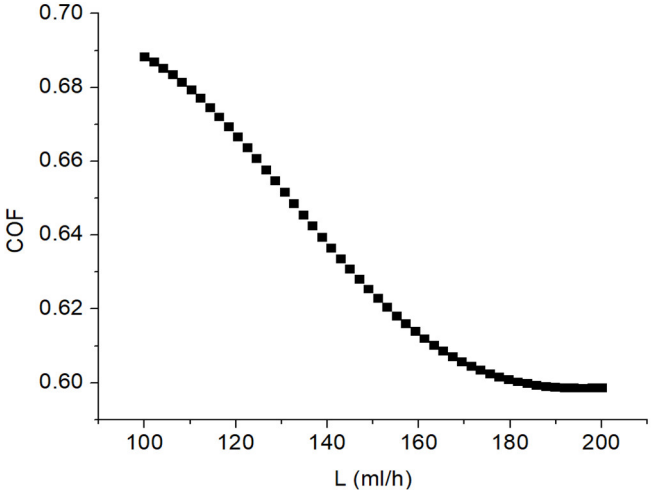


(b) COF versus L

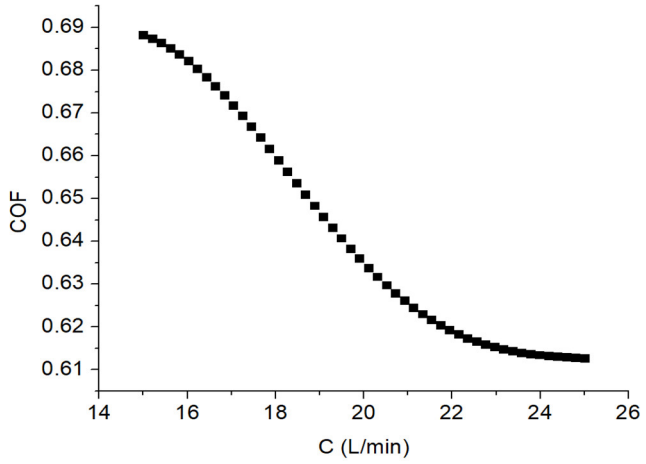


(b) COF versus C

Figure 10. The main impacts of LCMQL parameters on the COF

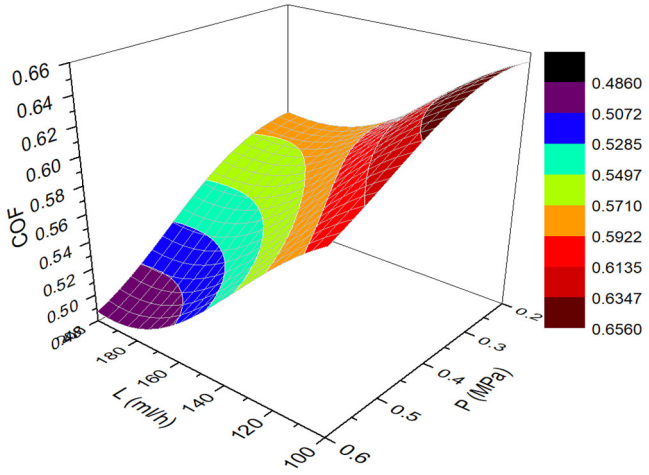


(a) COF vs P and L

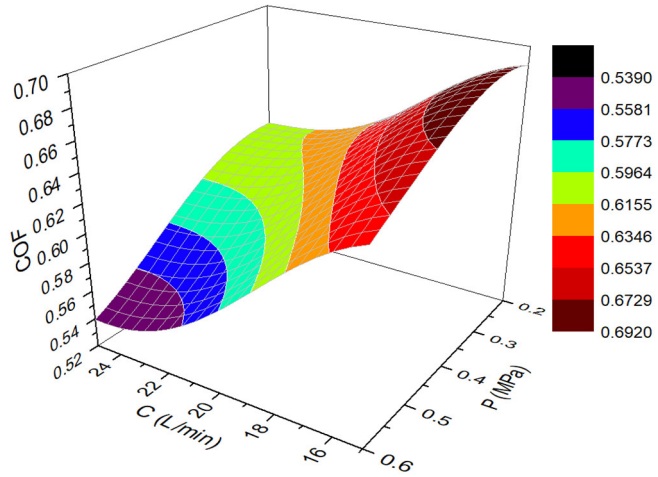


(b) COF vs P and C

Figure 11. The interactive impacts of LCMQL parameters on the COF

As shown in Fig. 10, lower *COF* values are obtained with higher LCMQL paramaters. The relative reductions in terms of the *P*, *L*, and *C* are 7.1%, 14.5%, and 11.5%, respectively. A higher *P* produces a low oil-mist's diameter, generating lower friction. A smoother surface is produced, leading to a reduction in the COF. A higher *L* increases lubricant entering the interface region, the material compression is smoothly executed. The roughness decreases, resulting in a low *COF*. A higher *C* produces a thin film at the interfaces, resulting in low friction. A smoother surface is generated, leading to a low *COF*. Fig. 11 presents the interactive impacts of LCMQL parameters on the *COF*.

As shown in Fig. 12, higher *PM10* values are found with increased LCMQL parameters. The relative increases in terms of the *P*, *L*, and *C* are 300.2%, 528.6%, and 351.4%, respectively. A higher *P* produces low oil-mist's diameter and increases its velocity, leading to higher amount of particulate matter; hence, the *PM10* increases. A higher *L* increases amount of the oil in the air; hence, the *PM10* increases. A higher *C* increases the amount of liquid $CO_2$ penetrating the burnishing region, leading to an increased *PM10* under the impact of the machining temperature. Fig. 13 presents the interactive impacts of LCMQL parameters on the *PM10*.

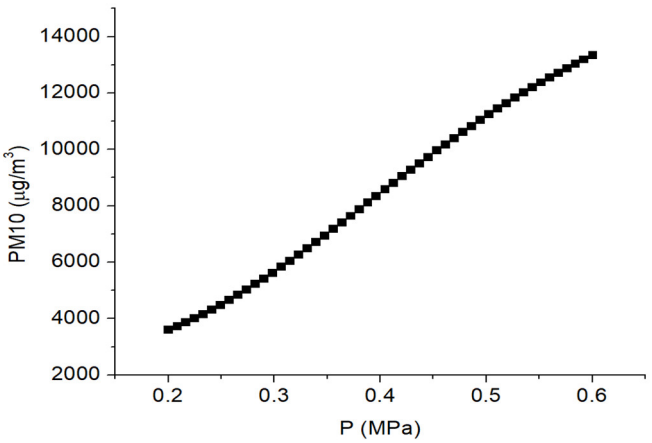


(a) PM10 versus P

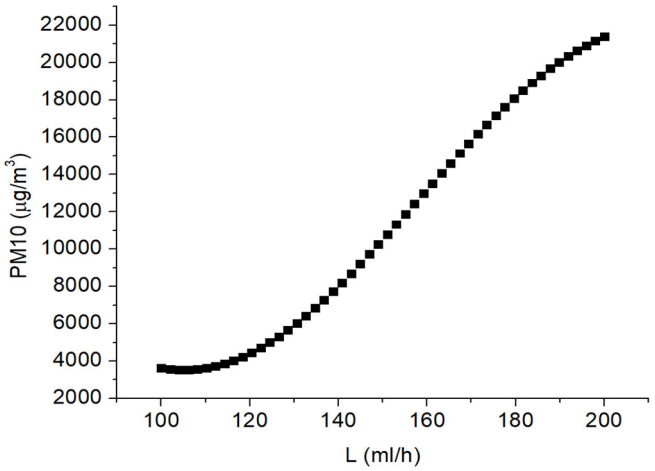


(b) PM10 versus L

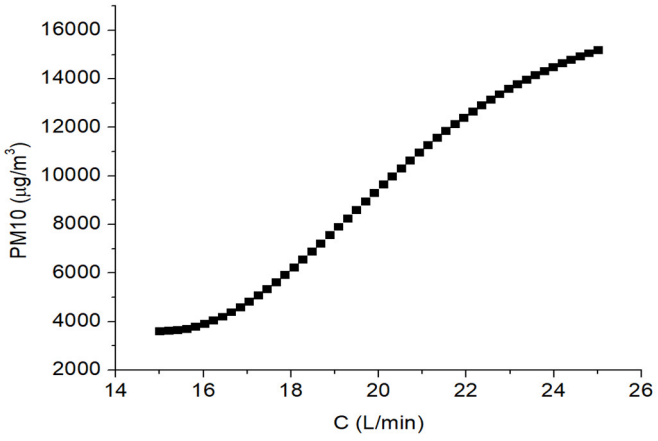


(c) PM10 versus C

Figure 12. The impacts of LCMQL parameters on the PM10

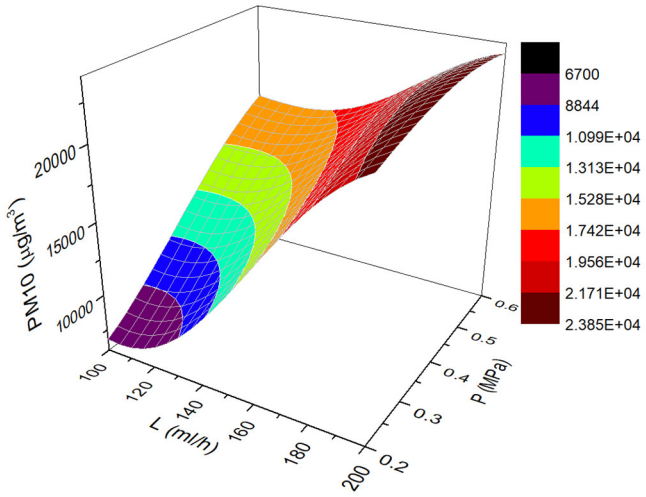


(a) PM10 vs P and L

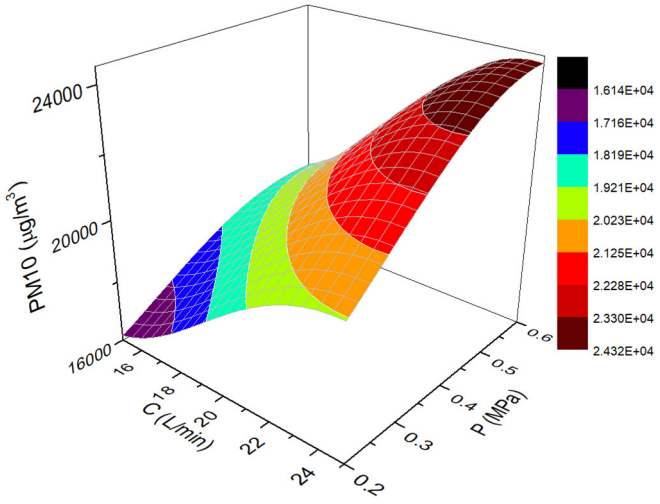


(b) PM10 vs P and C

Figure 13. The interactive impacts of LCMQL parameters on the PM10

### 4.3. Optimal data

The computed weights of the *COF* and *PM10* are 0.32 and 0.68, respectively. Fig. 14 depicts the graphical correlations among burnishing responses. The best results produced by the *P*, *L*, and *C* are 0.6MPa, 150ml/h, and 17L/min, respectively (Table 6). It was found that the *COF* and *PM10* are decreased by 5.9% and 22.3%, respectively, as compared to the user-defined values. The *COF* of the burnished surface under the effect of burnishing operation is reduced by 22.6%, as compared to the milled one.

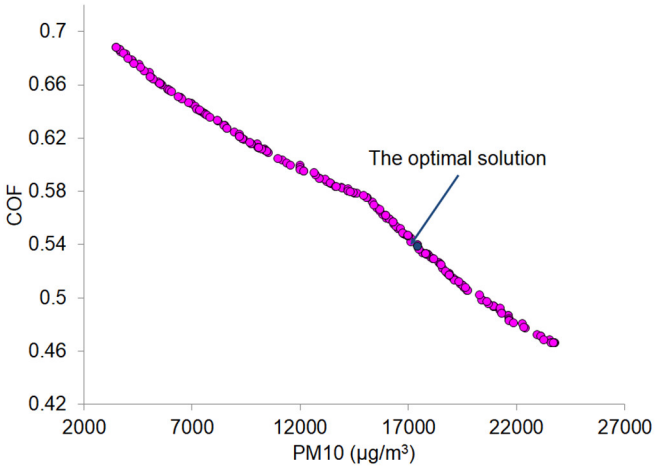


Figure 14. Pareto fronts produced by the DA

Table 6. Optimization results produced by the IDA

| Method | Optimization parameters | | | Responses | |
|---|---|---|---|---|---|
| | *P* (MPa) | *L* (ml/h) | *C* (L/min) | *COF* | *PM10* (µg/m³) |
| Initial values | 0.4 | 200 | 15 | 0.572 | 22424 |
| IDA | 0.6 | 150 | 17 | 0.538 | 17420 |
| Reductions (%) | | | | 5.9 | 22.3 |

## 5. CONCLUSIONS

In this work, a novel flat burnishing operation using liquid $CO_2$ and MQL was developed for machining SKD61 steel. The operating factors, including the *P*, *L*, and *C* are optimized to reduce the *COF* and *PM10*. The XGBoost models, MEREC, and DA were used to find optimality. Based on the obtained results, the obtained findings can be expressed as:

1. The OXGBoost correlations could be effectively utilized to model complex data and predict burnishing responses with acceptable accuracy.

2. Higher *P*, *L*, and *C* could be used to reduce the *COF*. Lower *P*, *L*, and *C* could be applied to decrease the *PM10*.

3. The *COF* was principally affected by the *L*, while the *P* and *C* had fewer impacts. The *PM10* was principally affected by the *L*, while the *C* and *P* had fewer impacts.

4. The computed weights revealed that the *PMI* had a higher importance than the *COF*.

5. The optimized outcomes of the *P*, *L*, and *C* were 0.6MPa, 150ml/h, and 17L/min, respectively. The *COF* and *PM10* were reduced by 5.9% and 22.3%, respectively.

6. The proposed DA can be utilized to deal with complicated issues for different burnishing operations.

**REFERENCES**

[1]. Rotella G., Rinaldi S., Filice L., "Roller burnishing of Ti6Al4V under different cooling/lubrication conditions and tool design: Effects on surface integrity," *Int. J. Adv. Manuf. Technol.*, 106: 431-440, 2020

[2]. Van A.L., Nguyen T.T., "Investigation and Optimization of MQL system parameters in the roller-burnishing process of hardened steel," *Stroj. Vestn./J. Mech. Eng.*, 68: 155-165, 2022.

[3]. Cagan S.C., Tasci U., Pruncu C., Bostan B., "Investigation of the effects of eco-friendly MQL system to improve the mechanical performance of WE43 magnesium alloys by the burnishing process," *J. Braz. Soc. Mech. Sci. Eng.,* 45: 22, 2023.

[4]. Cagan S.C., "Surface quality and environmental impact analysis of ball burnishing on Al8090 Aluminum-Lithium Alloy," *Materials*, 18: 1252, 2025.

[5]. Nguyen T. T., Nguyen T. A., Trinh Q. H., Le X. B., "Multi-performance optimization of multi-roller burnishing process in sustainable lubrication condition," *Mater. Manuf. Process*., 37(4): 407-427, 2021.

[6]. Nguyen T.T., Nguyen T.A., Dang X.B., Van A.L., "Multi-performance optimization of the diamond burnishing process in terms of energy saving and tribological factors," *P. I. Mech. Eng. E-J. Pro.,* 238: 2714-2727, 2023.

[7]. Sachin B., Narendranath S., Chakradhar D., "Application of desirability approach to optimize the control factors in cryogenic diamond burnishing," *Arab. J. Sci. Eng*., 45: 1305-1317, 2020.

[8]. Huang B., Kaynak Y., Sun Y., Khraisheh M. K., Jawahir I. S., "Surface layer modification by cryogenic burnishing of Al 7050-T7451 Alloy with near ultra-fine grained structure," *J. Manuf. Sci. Eng.,* 144: 031002, 2022.

[9]. Van A. L., Nguyen T. A., Dang X.B., Nguyen T.T., "A sustainable approach-based optimization of internal diamond burnishing operation," *Bull. Pol. Acad. Sci. Tech. Sci.,* 72: e151953, 2024.

[10]. Maximov J., Duncheva G., Anchev A., Dunchev V., Anastasov K., Argirov Y., "Sustainable diamond burnishing of Chromium-Nickel austenitic stainless steels: Effects on surface integrity and fatigue limit," *Appl. Sci.*, 14: 9031, 2024.

[11]. Van A.L., Nguyen T.T., "Machine learning-based optimization of diamond burnishing parameters in terms of energy efficiency and quality indexes," *Arab. J. Sci. Eng.,* 50: 9339-9363, 2024.

[12]. Maximov J., Duncheva, G., Anchev A., Dunchev V., Argirov Y., "Improvement in fatigue strength of Chromium-Nickel austenitic stainless steels via diamond burnishing and subsequent low-temperature gas nitriding," *Appl. Sci.*, 14: 1020, 2024.

[13]. Sachin B., Narendranath S., Chakradhar D., "Enhancement of surface integrity by cryogenic diamond burnishing toward the improved functional performance of the components," *J. Braz. Soc. Mech. Sci. Eng.,* 41: 396, 2019.

[14]. Kudva S. A., Anne G., Ramesh S., Sharma P., Jagadeesh C., Ritti L., Naik G., Deepar G. D., "Enhancing surface characteristics of Mg-Zn-Sr alloy through cryo-ball burnishing; modeling and experimentation," *J. Mech. Sci. Technol*., 38: 1175–1185, 2024.

[15]. Hou W., Lou N., Wang H., Cai Z., Xing Z., Piao Z., "Research on the microstructure and corrosion-wear resistance mechanism of Ti-6Al-4V alloy under cryogenic burnishing," *J. Mater. Res. Technol.,* 35: 5854-5871, 2025.

[16]. Kumar A., Ramadas H., Samal B. B., et al., "Laser polishing of cobalt chrome alloy fabricated by laser powder bed fusion process: design of experiment-based approach for reducing surface roughness," *Int J Adv Manuf. Technol*., 134: 1245-1264, 2024.

[17]. Souaidi C., Yallese M. A., Amirat A., et al., "Analysis, modelling and optimization during sustainable Dry and MQL turning of AISI 52100 steel using DF, GRA, EAMR, EDAS and FUCA methods," *Int J Adv Manuf. Technol*., 135: 5035-5069, 2024.

[18]. Benchekroun M.T., Zaki S., Aboussaleh M., et al., "Development of a kiln petcoke mill predictive model based on a multi-regression XGBoost algorithm," *Int J Adv Manuf. Technol.,* 130: 3373-3386, 2024.